A METHOD FOR THE COUPLING OF COMPRESSIBLE 3D FLOW SIMULATIONS WITH A CAVITATION EROSION MODEL FOR DUCTILE MATERIALS AND ASSESSMENT OF THE INCUBATION TIME

Felix Schreiner*, Stephan Mottyll and Romuald Skoda

Chair of Hydraulic Fluid Machinery
Ruhr-University Bochum
Universitätsstraße 150, 44801 Bochum, Germany
web page: www.hsm.rub.de
* Corresponding author, e-mail: felix.schreiner@ruhr-uni-bochum.de

Key words: 3D CFD, OpenFOAM, cavitation erosion, erosion model, incubation time

Abstract. A compressible 3D in-house flow solver with temporal nanosecond resolution is coupled to a simple material erosion model for ductile materials. Due to limited spatial resolution, not all details of collapsing wall adjacent single bubbles can be resolved, and thus a collapse detection algorithm based on the mass flux divergence is applied. Load collectives are statistically evaluated by the multitude of detected collapses and serve as input for the material model. Grid dependence is carefully assessed. Since the physical simulation time is much shorter than the realistic exposure time, a method for the time extrapolation of the wall load to capture realistic time scales together with a step-by-step implementation is presented. The simulation method is applied on an impinging water jet test case as well as on an ultrasound cavitation case. A validation on temporally highly-resolved pressure measurement data is performed. Limitations of the particular material model are pointed out. The coupled CFD – material model comprises one model parameter, in terms of the cell size of a reference computational grid to handle grid dependence, that needs to be case-dependently fixed e.g. on measurement data. We conclude, that for a more predictive method, the detailed spatial resolution of single bubble collapses seems indispensable.

1 INTRODUCTION

Hydrodynamic cavitation is the development of voids in liquids by local depressurization below a critical pressure [1], e.g. induced by flow acceleration at propellers. As the ambient liquid pressure around the voids increases again further downstream, re-condensation leads to violent void collapses resulting in shock waves. In wall-adjacent flow regions, micro-jets in the collapsing bubbles act on the wall and induce high peak loads that may lead to material failure after a certain time. Besides vibration and noise it is cavitation erosion that causes serious issues in marine engineering applications and may limit the lifetime of ship propulsion units.

The damage potential of cavitation has been well recognized by both physicians and engineers, so that significant efforts have been made for the assessment of erosion sensitive wall zones by CFD methods. Besides the qualitative prediction of flow aggressiveness and erosion sensitive wall zones, it is of increasing interest for the design of propulsion units to determine the temporal evolution of erosion-induced damage and to assess the time to failure, i.e. the incubation time, what is the aim of the present study.

The cavitating flow in propulsion units can be approximated by simplified geometries, which can be better controlled in a lab environment than rotating propellers. This study focuses therefore on two standardized test cases, an axisymmetric nozzle as well as an ultrasonic horn test facility. In the axisymmetric nozzle, a jet impinges a wall and is accelerated and radially redirected, leading to cyclic shedding ring-shaped cavitation clouds and a ring-shaped erosion pattern [2–4]. Different CFD methods have been employed for the assessment of the flow aggressiveness on that test case. Mihatsch et al. [5–7] presented the assessment of erosion sensitive wall zones by a compressible CFD method and a collapse detection algorithm. Mottyll [8] has reproduced these results by our in-house implementation of essentially the same numerical scheme. Additionally, Mottyll [8] has assessed erosion sensitive wall zones by a more simple method as proposed by Skoda et al. [9]: By counting events exceeding threshold values for wall pressure and void collapse rate, erosion indicators and a map of dimensionless erosion probability are obtained. Koukouvinis et al. [10] are considering the temporal derivative of the void fraction to introduce erosion indices for the assessment of erosion sensitive wall zones. Peters et al. [11] deduced a dimensionless erosion intensity from a micro-jet model, validated it on the axisymmetric nozzle case and applied this method to a ship propeller [12].

The ultrasound cavitation test case is standardized for material erosion resistance tests according to ASTM G32 (American Society for Testing and Materials) [13]. Cavitation is generated by an oscillation horn tip at $f_{\mathrm{drive}} \approx 20\,\mathrm{kHz}$ and shows void dynamics similar to hydrodynamic cavitation [14, 15]. The ring-shaped erosion sensitive wall zones are well predicted by [15, 16], and different erosion mechanisms at horn tip and stationary specimen are revealed [15]. Besides the common incubation time measurements [17], a direct assessment of flow aggressiveness by pressure measurements has been presented by Paepenmöller et al. [18].

In these exemplary cited studies a good prediction of erosion sensitive wall zones as a qualitative measure of cavitation erosion could be obtained. However, no parameters of the solid material have been considered in these simulations. For the incubation time assessment as a quantitative measure, a model for the material response to cavitation impacts needs to be considered. For the axisymmetric nozzle test case, Mihatsch et al. [7, 19] have presented an assessment of the incubation time by a coupling of their CFD code with a simple material model [2]. We adopt that procedure in the present study and evaluate its applicability for an ultrasonic horn test case. We present a method for the time extrapolation of the wall load to capture realistic time scales. Furthermore, we provide a step-by-step implementation of the coupling of the CFD code, i.e. collapse load collectives deduced from the flow solution, with the material model. The coupled CFD method and material model is referred to as erosion model in what follows. Additionally specific limitations of the material model are pointed out.

The paper is organized as follows. In section 2, the flow solution method together with the numerical setups as well as the evaluation of single collapses and collapse load collectives are presented. In section 3, we present the flow solver validation on pressure measurement data. In

section 4, the material model and its coupling to the flow solver by collapse load collectives is illustrated. Results in terms of incubation time are discussed for the axisymmetric nozzle and ultrasonic horn test cases. Our conclusions in regard of future marine applications and model improvements are drawn in section 5.

2 METHODOLOGY

2.1 Flow Solver

For the resolution of void collapses, a compressible flow solver and a time resolution in the range of nanoseconds needs to be employed. Thus, the density-based low Mach number consistent Godunov-type numerical scheme by [20, 21] has been adopted, that was designed for resolving pressure wave dynamics and shocks in cavitating flows. We perform an explicit Runge-Kutta time integration and a finite volume discretization of the Euler equations for an inviscid fluid, coupled with an isentropic barotropic equation of state neglecting non-dissolved gas. A homogeneous mixture of liquid and vapor at thermodynamic equilibrium within each cell is assumed.

Details of the flow solver and our native in-house block-structured implementation `hydRUB` can be found in [8,15,22]. Results of the present study have been obtained with our unstructured OpenFOAM implementation of the solver, referred to as `hydRUBFoam` [18, 23]. For density, the MINMOD reconstruction scheme [24] is employed, while for velocity the GammaV scheme [25] is utilized to provide 2nd order accuracy. Further details on the flow solver can be found in [8, 15, 18, 22, 23].

2.2 Test Cases and Numerical Setup

The axisymmetric radial nozzle test case is sketched in Fig. 1a, together with the numerical setup. The nozzle flow strikes onto a target disc (i.e. the lower wall) and is redirected radially outward into the small gap between upper and lower wall. A ring-shaped erosive zone occurs at the target disc within a radius range of about $r \approx 19...27\,\mathrm{mm}$ [26]. Measured incubation times are taken from [2, 7]. The numerical setup has been adopted from [6, 7] and is summarized in Table 1, together with the operation conditions. A grid study is performed with a refinement of the inner grid region (referred to as *analysis domain* in Fig. 1a), while the outer grid is left unchanged and connected by non-matching interfaces, i.e. hanging nodes.

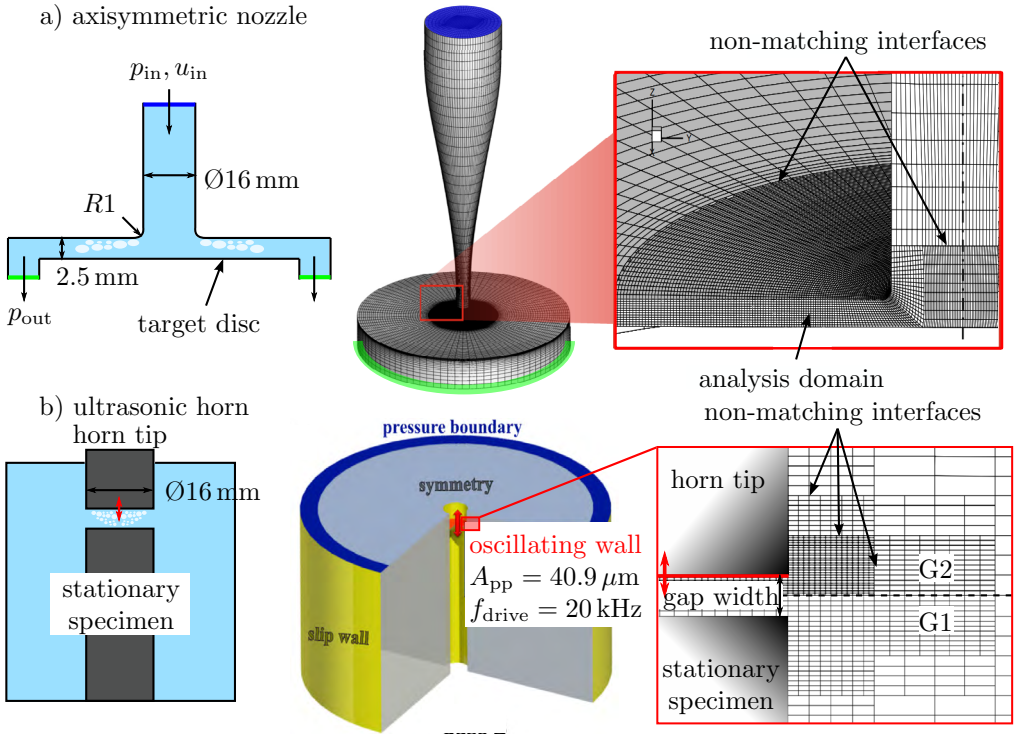

Figure 1: Illustration of the axisymmetric nozzle and the ultrasonic horn test case with the numerical setups

The ultrasonic horn test case (see Fig. 1b) is operated at 19.8 kHz horn driving frequency and 40.9 μm peak-to-peak amplitude. The horn tip is immersed into distilled water at equilibrium air saturation, kept at 20°C by an actively controlled indirect cooling circuit. The gap width between horn tip and the stationary specimen equals 0.5 mm. The numerical setup has been adopted from [15, 18, 22] and is summarized in Table 1. Two spatial resolutions have been employed for a grid study. The computational grids G1 and G2 with hanging-node configuration are depicted in Fig. 1b.

Table 1: Operation and setup parameters of the axisymmetric nozzle and the ultrasonic horn test case

axisymmetric nozzle		
inlet pressure	40 bar	
outlet pressure	18.9 bar	
inlet velocity	1.37 m·s^{-1}	
grid	G1	G2
total numb. of cells [-]	382 000	2 393 000
numb. cells in gap [-]	12	24
num. time step [ns]	30.2	19.1
sim. phys. time [ms]	∼ 359	∼ 86

ultrasonic horn		
peak-to-peak amplitude	40.9 μm	
frequency	19.8 kHz	
gap width	0.5 mm	
grid	G1	G2
total numb. of cells [-]	105 000	329 000
numb. cells in gap [-]	8	16
num. time step [ns]	16.8	8.1
sim. phys. time [ms]	∼ 163	∼ 85

2.3 Collapse Detection and Load Collectives

The flow solver (see section 2.1) has been shown to reproduce the dynamics of collapsing wall adjacent single bubbles, i.e. micro-jet formation and torus-shaped shock wave, given that the spatial resolution is sufficiently high [27, 28]. For the simulation of macroscopic test cases as the axisymmetric nozzle and the ultrasonic horn, such a bubble-resolving spatial resolution is not feasible due to tremendous computational effort. Thus, we account for collapses and peak pressures of distinct voids in a certain vicinity of the wall by a mass flux divergence criterion proposed by Mihatsch et al. [5, 6]. Albeit we may not resolve the collapse of each microscopic bubble, we resolve void collapses down to a scale that is just in the range of our spatial resolution, and we refer to that procedure as meso-scale simulation. In order to cope with the limited spatial resolution, grid dependence is treated by the projection of the collapse pressure p_{coll} to a reference grid with yet arbitrary reference cell length x_{ref} [6], and a corrected collapse pressure p_{corr} is obtained according to eq. 1.

$$p_{\mathrm{corr}} = \frac{\sqrt[3]{V_{\mathrm{cell}}}}{x_{\mathrm{ref}}}\, p_{\mathrm{coll}} \tag{1}$$

The occurrence of collapses in terms of the cumulated collapse rate *ccr* is corrected by eq. 2 and the introduction of the empirical parameter $\kappa = 3/2$ [6].

$$ccr_{\mathrm{corr}} = \left(\frac{\sqrt[3]{V_{\mathrm{cell}}}}{x_{\mathrm{ref}}}\right)^{\kappa} ccr \tag{2}$$

By a statistical evaluation of a multitude of collapses, collapse load collectives are obtained in terms of the cumulated collapse rate *ccr* vs. collapse pressure p_{coll}. Details of this evaluation method are described in [15]. Exemplary collapse load collectives are illustrated in Fig. 2 for the erosion-prone wall region of the axisymmetric nozzle, defined as a somewhat arbitrary wall adjacent layer $dz_{\mathrm{wall}} < 500\,\mu$m normal to the bottom wall and a ring segment of $\Delta r = 19...32$ mm. According to Schmidt et al. [29], a void collapse that occurs within the fluid domain in a certain distance from the wall, emits a pressure wave that reaches the wall, and the resulting maximum wall pressure is essentially grid-independent. Nevertheless, according to [15], we do not perform a projection of detected collapses to the wall, since it is the collapses that occur in the immediately wall-adjacent cell layer that primary contribute to high wall loads. As this wall-adjacent cell layer on the fine computational grid is not present on the coarse grid, a significant grid dependence remains after wall projection of the collapse pressure [15]. Thus, all collapse events within the erosion-prone wall region are considered to be representative for the wall load, without projection to the wall. This procedure is equivalent to the assumption that the pressure peak of each detected collapse acts immediately on the wall, irrespective of its actual wall distance. It is noteworthy that this procedure slightly deviates from the one by [7], who introduced a wall projection of collapse pressure with the maximum value of either x_{ref} or the wall distance of a collapse occurrence. As can be seen in Fig. 2, the grid dependence of the uncorrected load collectives (no corr.) is effectively compensated by the projection to a reference grid x_{ref} (eq. 1) and by the rate correction (eq. 2). After correction, the load collectives of both grids essentially match and can be approximated by a trendline for each value of x_{ref}. An appropriate value of x_{ref} is yet undetermined, a fact that will be addressed in section 4.3.

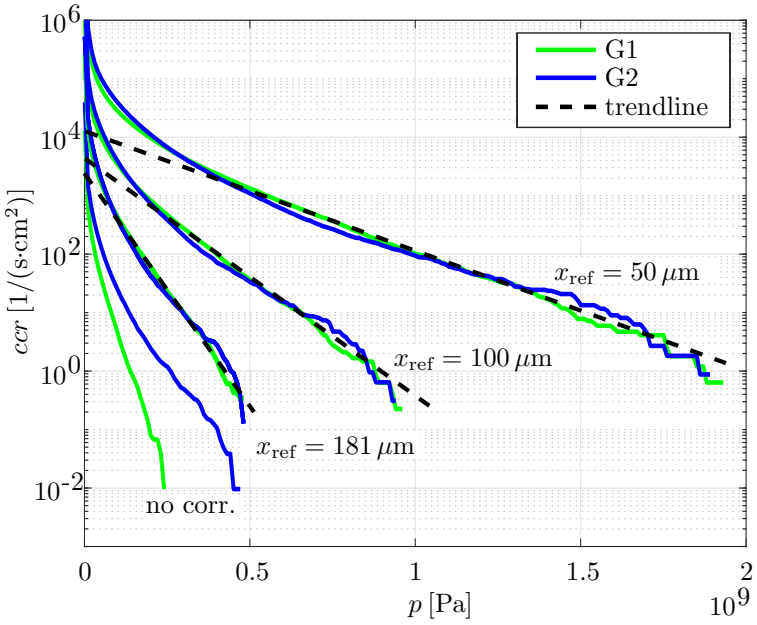

Figure 2: Exemplary collapse load collectives for the axisymmetric nozzle without correction (no corr.) and with correction according to eqs. 1 and 2 with different scaling parameters x_{ref}

3 VALIDATION BY PRESSURE MEASUREMENTS

In a proceeding study [18] we performed temporally high-resolved wall load measurements with Ø5.0 mm polyvinylidene fluordide (PVDF) pressure sensors flush-mounted in the erosion sensitive wall region of the stationary specimen. Due to the relatively large sensor size, we label the load as *force* instead of *pressure*. We evaluated the results statistically in terms of force load collectives, i.e. cumulative force rate cfr vs. measured sensor force (not to be confused with collapse load collectives in terms of ccr vs. collapse pressure, see Fig. 2) and compared CFD results by a virtual sensor to the measurements. The force load collectives in the simulation were essentially grid-independent and matched the measured force load collectives with a very good accuracy for different gap widths [18].

Regarding the axisymmetric nozzle test case, Franc et al. [4] performed wall pressure measurements by a commercial piezoelectric sensor with Ø3.6 mm in the erosion sensitive ring-shape zone at the target disc. In their simulations, Mihatsch et al. [6] reproduced this experiment by a virtual pressure sensor, found a significant grid dependence of the sensor force load collectives and performed an analogous projection to a reference grid as has been proposed for the collapse load collective by eq. 2. By matching their virtual sensor results to measured force load collectives, the value of x_{ref} has been fixed to a value of 181 μm. This value of x_{ref} has subsequently been applied also to the collapse load collective. Thus, x_{ref} is fixed by this calibration procedure. We could reproduce the procedure by Mihatsch et al. [6] with our in-house solver implementations `hydRUB` [8] as well as `hydRUBFoam` and ended up at essentially the same value of $x_{\mathrm{ref}} = 181\,\mu$m. The corresponding collapse load collective is also depicted in Fig.2.

Obviously, the grid dependence of force load collectives at the axisymmetric nozzle test case

plays a decisive role for the fixing of x_{ref}. As stated above we did not observe an appreciable grid dependence in our ultrasonic horn simulations [18], where larger sensors Ø5 mm have been used. Therefore, we systematically vary the sensor size of the axisymmetric nozzle case by splitting a ring-shaped virtual sensor in circumferential portions as illustrated in Fig. 3a. It is noteworthy that the simplification of the sensor geometry from circular shape to a ring segment is without any significance, since in radial sensor extent direction a statistically homogeneous load is present [8]. The resulting force load collectives in Fig. 3b indicate that the grid dependence is in fact decreasing for larger sensor areas. For a sensor area of about $A_{\mathrm{sensor}} = 18.5\,\mathrm{mm}^2$ and larger, the force load collective is essentially grid independent. We made an equivalent observation in preliminary ultrasonic horn simulations, where we successively scaled-down the virtual sensor and observed an increasing grid dependence towards smaller virtual sensors. It can be concluded that for increasing sensor area size, the single punctual peak loads are increasingly averaged out over more cell faces, leading to an increasing grid-independence. It is also noteworthy that for their x_{ref} fixing on a Ø3.6 mm sensor, Mihatsch et al. [6] applied grid resolutions with cell face numbers that correspond to our $A_{\mathrm{sensor}} = 10\,\mathrm{mm}^2$, where we still observe a significant grid dependence according to Fig 3b. It will be interesting to see whether for finer grids, the grid dependence will diminish for the Ø3.6 mm sensor. That will be investigated in further studies.

The sensor size variation reveals that the grid dependence of force load collective and thus the fixing of x_{ref} are significantly affected by the sensor size. We therefore prefer to immediately determine x_{ref} by incubation time measurements as will be discussed in what follows.

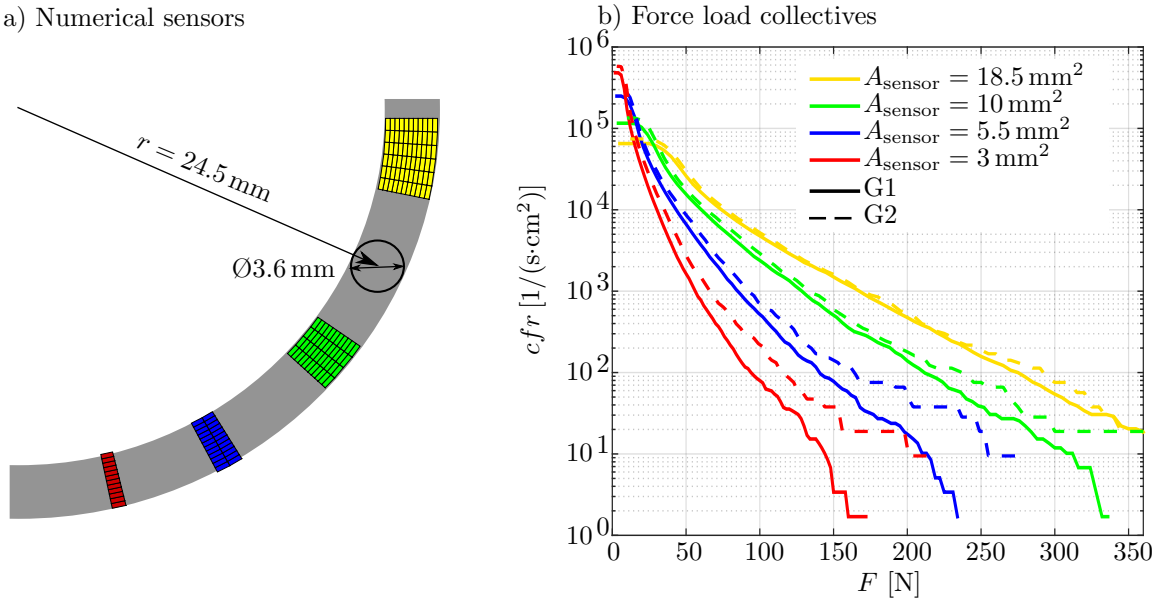

Figure 3: Size variation of exemplary virtual sensors (a) with resulting force load collectives (b)

4 ASSESSMENT OF INCUBATION TIME

4.1 Material Model

Franc et al. [2] proposed a simple one-dimensional erosion material model for ductile steels. The erosion process is based on the accumulation of plastic material deformation and successive work hardening up to material failure, determining the incubation time. The key assumption of the model involves, that the absorbed energy can be successively accumulated for each collapse impact until fracture limit at the ultimate strain is reached [30]. Strain rate effects and loads below the yield strength of the material are neglected. In the original intention of the material model [2], flow aggressiveness is evaluated by statistical analyses of experimental pitting results in terms of impact rate, mean load and mean impact area, which serve as input data for the material model. Further model approaches e.g. [31, 32] assume a ductile deterioration of the material by micro cavities and creeping. Hattori et al. [17, 33, 34] proposed a material model accounting for high cycle fatigue mechanisms. Although these exemplary cited material models comprise physically sound assumptions, we prefer in a first step to couple the ductile model by Franc et al. [2] to the CFD code due to its plainness and because the flow-induced load can be prescribed in a straightforward way, which is presented in the subsequent section.

4.2 Coupling of Load Collectives and Material Model

We start with a brief summary of the material model, details can be found in [2]. It is assumed that the material response to a specified load follows the stress-strain relationship of Ludwig-type:

$$\sigma(\varepsilon) = \sigma_{\mathrm{Y}} + K\,\varepsilon^{n} \tag{3}$$

The yield stress σ_{Y}, strength index K and strain hardening exponent n are specific for each material and obtained by tensile tests. For successive impacts and a progressive surface hardening, the resulting one-dimensional strain profile is approximated by a one-dimensional power law:

$$\varepsilon(x) = \varepsilon_0 \left(1 - \frac{x}{l}\right)^{\theta} \tag{4}$$

ε_0 is the strain at the surface ($x = 0$) and x the distance to the surface. l is the thickness of the hardened layer, which progressively increases with exposure time, until it reaches a maximum thickness L. The metallurgical parameters L and the shape factor Θ are determined from microhardness measurements in a cross-section of an eroded sample. The energy that is absorbed for a strain ε_i can be formulated as:

$$W(\varepsilon_i) = \int_{x=0}^{l} \left[\int_{\varepsilon=0}^{\varepsilon(x)} \sigma \, d\varepsilon \right] \bar{S}\, dx = \varepsilon_i\, \bar{S}\, L \left(\frac{\varepsilon_i}{\varepsilon_{\mathrm{U}}}\right)^{1/\theta} \frac{\sigma_{\mathrm{Y}} + \beta\, K \varepsilon_i^{n}}{1+\theta} \tag{5}$$

$$\text{with:} \quad \beta = \frac{1+\theta}{(1+n)(1+\theta+n\theta)}$$

$\bar{S}$ is the mean impact area and has been obtained by a statistical pit analysis in the experiment [2], together with a mean load $\bar{\sigma}$ and a mean impact rate $\dot{N}$. In our CFD approach, no mean value of $\bar{\sigma}$, but the entire spectrum of collapses is taken into account for the evaluation of

$W(\sigma_i)$. First, $W(\sigma_i)$ is obtained from $W(\varepsilon_i)$ by inserting eq. 3 into eq. 5. $W(\sigma_i)$ is the absorbed energy given by a stress σ_i. The basic idea is, that, as soon as the accumulated energy (obtained by summing up the distinct values of $W(\sigma_i)$) exceeds the fraction energy $W(\sigma_\mathrm{U})$, the incubation time has been achieved. σ_U is the ultimate strength of the material and obtained from tensile tests. The spectrum of σ_i is obtained from our CFD collapse load collectives. In what follows, we provide a summarized step-by-step algorithm. The steps are illustrated in Fig. 4.

(1) The radial direction is discretized into ring zones with radial position r_pos and a radial width Δr_ring. The distinct rings may overlap. In order to provide a radial variation of collapse load collectives, the detected collapses are filtered so that they are located within the radial ring zone. Only collapses in a certain wall vicinity $< dz_\mathrm{wall}$ are taken into account. Δr_ring must be chosen large enough to provide a sufficient statistic of collapses. A further constraint that requires rather small values of dz_wall is to represent a certain wall vicinity. Values of Δr_ring and dz_wall are provided further below when the results are discussed.

(2) The collapse load collectives are projected to a reference grid x_ref according to eqs. 1 and 2.

(3) Frequent collapses with low pressure and seldom collapses with high pressure are sorted out to provide a unique trendline (step 4). A minimum pressure level p_min and a minimum rate $count_\mathrm{min}$ are empirically prescribed. Values of p_min and $count_\mathrm{min}$ are provided in the result section. Note that $count_\mathrm{min}$ is applied to the total number of collapse occurrences in the simulation time interval and is not concerned by the projection to the reference grid x_ref. $count_\mathrm{min}$ is applied to the rate before the rate correction in terms of eq. 2. On the other hand, p_min is applied to the corrected pressure p_corr, i.e. after evaluation of eq. 1.

(4) By the filtered collapse load collectives according to step 3, a linear regression is obtained for each radial zone with the fitting parameters A and B:

$$ccr_\mathrm{corr}(p_\mathrm{corr})\,[1/(\mathrm{s}\cdot\mathrm{cm}^2)] = \left[(10^A)^{p_\mathrm{corr}}\cdot 10^B\right] \tag{6}$$

$ccr_\mathrm{corr}(p_\mathrm{corr})$ represents a rate of collapses per unit surface area and unit time.

(5) Each single impact affects only a small area A_impact. We assume the $ccr_\mathrm{corr}(p_\mathrm{corr})$ occurs with the same probability within each ring zone and set $A_\mathrm{impact} = \bar{S}$. According to [19], we set $\bar{S}$ in eq. 5 equal to the surface of a reference cell x_ref^2. Thus, we obtain the collapse rate for one uniform covering of a complete ring zone surface $ccr'(p_\mathrm{corr})$:

$$ccr'(p_\mathrm{corr})[\mathrm{s}^{-1}] = x_\mathrm{ref}^2\cdot ccr_\mathrm{corr}(p_\mathrm{corr}) \tag{7}$$

(6) $ccr'(p_\mathrm{corr})$ is temporally extrapolated to the number of collapses $ccr''(p_\mathrm{corr},T)$ for a time interval T:

$$ccr''(p_\mathrm{corr},T)\,[-] = ccr'(p_\mathrm{corr})\,[\mathrm{s}^{-1}]\cdot T = x_\mathrm{ref}^2\cdot T\cdot ccr_\mathrm{corr}(p_\mathrm{corr})\,[1/(\mathrm{s}\cdot\mathrm{cm}^2)]. \tag{8}$$

The dimensionless measure $ccr''(p_\mathrm{corr},T)$ represents the cumulative collapse rate for a specified physical time T acting on the impact area $\bar{S}$.

(7) Discrete loads i.e. $p_i = p_1, p_2, ..., p_m$ are obtained by regarding p_corr at integral values of $ccr'' = 1, 2, ..., m$. Since the ductile material model accounts only for loads above the yield strength and loads that occur at least once per covering, the discrete loads are filtered with $p_i \geq \sigma_\mathrm{Y}$ and $\min(ccr'') = 1$.

These discrete loads p_i correspond to σ_i and serve as input for the material model. The energy absorbed by the material is accumulated for all loads occurring within a time interval T:

$$W_{\mathrm{tot}}(T) = \sum_{i=1}^{m} W(\sigma_i) \tag{9}$$

When $W_{\mathrm{tot}}(T)$ approaches the fracture energy $W(\sigma_{\mathrm{U}})$, then T approaches the incubation time t_{inc}. The condition

$$W(\sigma_{\mathrm{U}}) - W_{\mathrm{tot}}(t_{\mathrm{inc}}) = 0 \tag{10}$$

is numerically solved for t_{inc} by a bisection method.

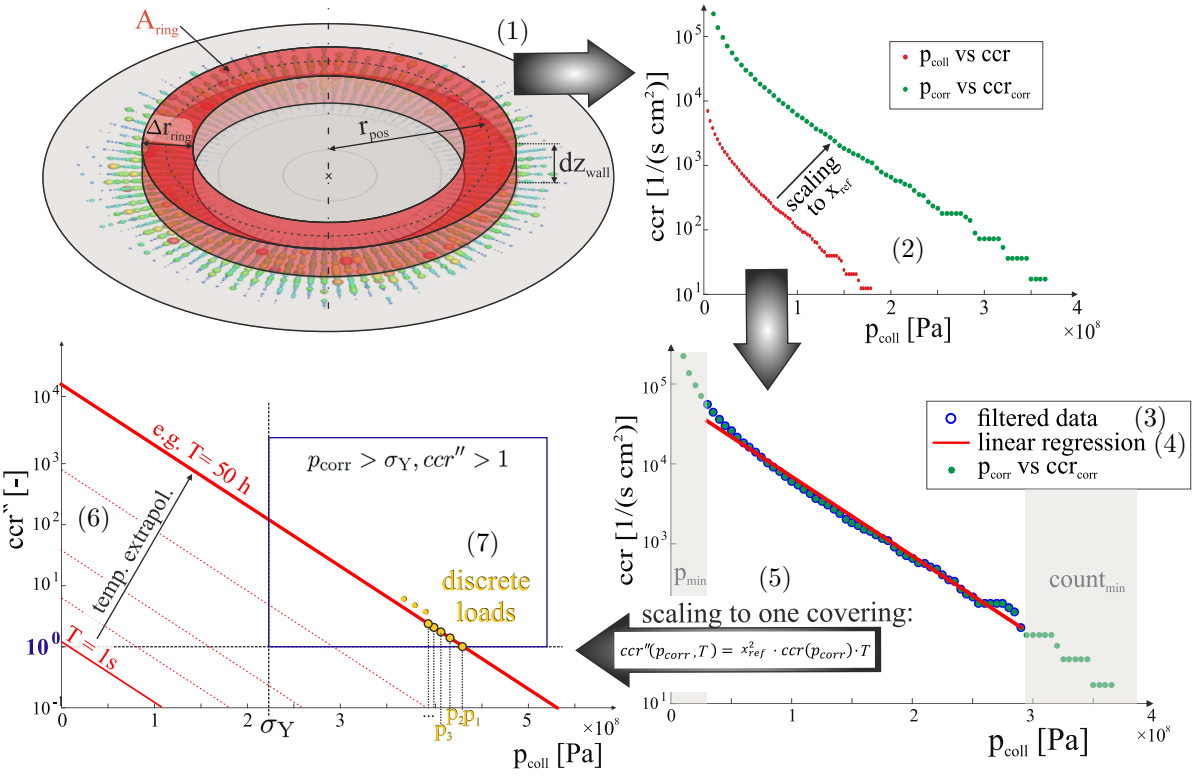

Figure 4: Schematic illustration of the load approximation from CFD results that serve as input for the material model

4.3 Results

4.3.1 Axisymmetric Nozzle

Based on preliminary studies [6–8, 19] we choose a range within $r = 20...41\,\mathrm{mm}$ for the discretization of radial zones with $\Delta r_{\mathrm{ring}} = 4\,\mathrm{mm}$ and $dz_{\mathrm{wall}} = 500\,\mu\mathrm{m}$. The resulting collapse load collectives are depicted in Fig. 5a for three exemplary radial positions. Collapse pressure and rate have been projected to a reference grid $x_{\mathrm{ref}} = 245\,\mu\mathrm{m}$ (this value will be explained further below) according to eqs. 1 and 2. As expected, the grid dependence could be effectively

minimized, so that a unique trendline in terms of a linear regression according to eq. 6 can be introduced. Seldom occurring collapses are marked by circles in Fig. 5a and have been selected out by choosing the threshold value $count_{\min} = 6$. $p_{\min}$ equals 50 bar. Based on these load collectives, the incubation time is assessed for the stainless steel SS-A2205 and a Nickel Aluminum Bronze alloy NAB. The material properties are summarized in Table 2.

In Fig. 5b, the radial distribution of the incubation time is depicted. The positions of the exemplary load collectives (Fig 5a) are marked by lines, so that the association between flow aggressiveness in terms of collapse load collectives and the incubation time gets obvious. Note that the load collective at $r = 26\,\text{mm}$ (red line) comprises a higher rate in terms of ccr_{corr} than the load collective at $r = 34\,\text{mm}$ (green line), but at the same time shows a slightly flatter slope. The latter might result in less violent collapses after temporal extrapolation according to eq. 8. Since the incubation time for $r = 26\,\text{mm}$ is lower than for $r = 34\,\text{mm}$, it can be concluded that both load collectives cross only at very high loads (not shown here) close to the fracture stress and the higher rate dominates over the lower slope resulting in a more aggressive flow situation at $r = 26\,\text{mm}$ than at the location $r = 34\,\text{mm}$. For a comparison with the measured incubation time, the radially minimum value of the simulation results is evaluated. The reference grid parameter x_{ref} is chosen in a way that it matches the measured incubation time for SS-A2205, $t_{\text{inc}} = 35\,\text{h}$ [7], resulting in $x_{\text{ref}} = 245\,\mu\text{m}$. Thus per definition, t_{inc} matches the measured value at $r = 27\,\text{mm}$ for SS-A2205.

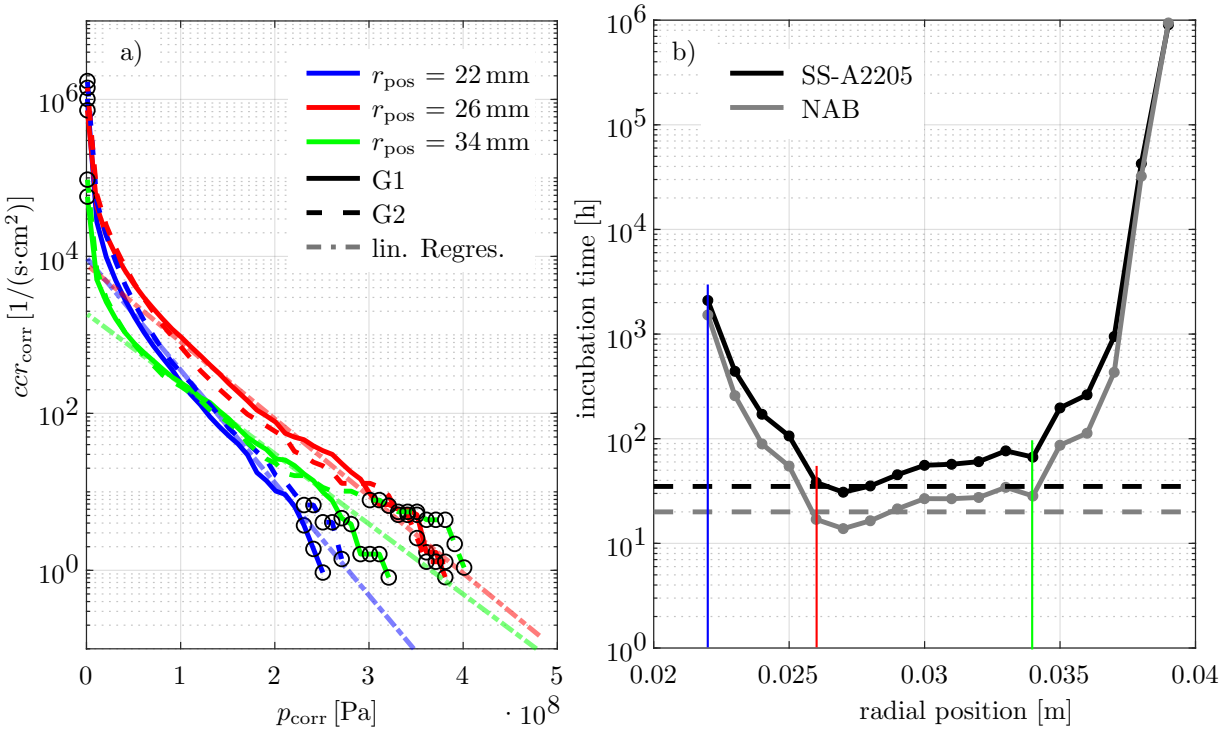

Figure 5: Collapse load collectives for exemplary radial positions for two grids G1 and G2 with regression according to eq. 6 (a) and the radial distribution of incubation time for two materials (b). The experimental incubation times are obtained from [7] and depicted as dashed lines.

According to the measurements by Chahine et al. [26], the erosion sensitive wall zones are located in a range of about $r \approx 19...27\,\mathrm{mm}$. While the minimum value of t_{inc} occurs at $r = 27\,\mathrm{mm}$ and is thus located just within that range, the region of high flow aggressiveness is predicted rather in a range of about $r = 25...34\,\mathrm{mm}$ and is thus shifted to higher radii. It is important to note that preliminary studies [7,8] on a different operation point ($p_{\mathrm{in}} = 21.3\,\mathrm{bar}$) have revealed an even more pronounced shift of low incubation time to a too large radial position. Mottyll [8] has evaluated the flow aggressiveness by erosion indicators [9] and found the same region of high flow aggressiveness $r = 21...28\,\mathrm{mm}$ compared to Koukouvinis et al. [10], although the incubation has been predicted too far downstream. By applying the erosion indicator method [9] by preliminary simulations in the present study, we could also confirm for $p_{\mathrm{in}} = 40\,\mathrm{bar}$ the correct location of high flow aggressiveness. Thus, the downstream shift of low incubation time can be attributed to the erosion modelling and not to shortcomings of the flow simulation: By the temporal extrapolation of the collapse load collective regressions from short simulated physical time (less than one second) to long incubation time (several hours), seldom occurring collapses with high collapse pressure might be artificially overvalued. This overvaluing of high-pressure collapses is further increased, since solely loads that exceed the material yield strength are considered by the ductile material model and thus loads in the macroscopic elastic region are a priori neglected. High cycle fatigue, however, may also contribute significantly to material failure [17, 34] and is completely neglected in our study by the use of a purely ductile material model [2].

In spite of these significant assumptions, we applied the material model to a second material in terms of NAB, also shown in Fig. 5b. Note that it is the same load collectives that enter the material model for both materials, only the material parameters according to Table 2 change. The incubation time for NAB is lower by a factor ~ 2 than for SS-A2205, which corresponds to the experimentally achieved ratio. Thus, the erosion model shows the proper qualitative answer to material properties.

Finally, it is noteworthy that a different reference grid size $x_{\mathrm{ref}} = 181\,\mu\mathrm{m}$, that has been proposed by [6, 7, 19] for the operation point $p_{\mathrm{in}} = 21.3\,\mathrm{bar}$, yields an incubation time one order of magnitude too low in our present investigation of $p_{\mathrm{in}} = 40\,\mathrm{bar}$. This makes the universal validity of the value of x_{ref} questionable, a conclusion that will be further supported by our ultrasound test case investigations that are presented in the subsequent subsection.

Table 2: Material parameters from tensile [3] and micro-hardness tests [26]

Material	σ_{Y}	σ_{U}	K	n	L	θ
SS-A2205	230 MPa	790 MPa	910 MPa	1/3.2	1.25 mm	2.2
NAB	355 MPa	683 MPa	1210 MPa	1/2.07	1.07 mm	2.8
316L	400 MPa	1020 MPa	900 MPa	1/2	0.2 mm	5

4.3.2 Ultrasonic Horn

The entire radial extent of the stationary specimen is discretized with $\Delta r_{\mathrm{ring}} = 2.5\,\mathrm{mm}$ and $dz_{\mathrm{wall}} = 200\,\mu\mathrm{m}$. As for the axisymmetric nozzle, $count_{\mathrm{min}} = 6$ and $p_{\mathrm{min}} = 50\,\mathrm{bar}$ have

been chosen. Stainless steel 316L is considered and the material parameters are summarized in Table 2. In Fig. 6, the radial distribution of the incubation time is depicted. The incubation time continuously increases towards larger radial locations and has its minimum in the specimen center, which is in agreement with radial distribution of flow aggressiveness, either evaluated by erosion indicators or a zonal evaluation of collapse load collectives [15]. The reference grid parameter x_{ref} is chosen in a way that it matches the measured incubation time $t_{\mathrm{inc}} = 2.25\,\mathrm{h}$ [18] for a zone with Ø5 mm in the specimen center, resulting in $x_{\mathrm{ref}} = 60\,\mu\mathrm{m}$. Note that in Fig. 6, the ring-shape discretization with the ring width of $\Delta r_{\mathrm{ring}} = 2.5\,\mathrm{mm}$ (as exemplary shown in blue) is resulting in a Ø5 mm area for the radial position $r = 1.25\,\mathrm{mm}$ (red), as each radial position is defining the center of inner and outer radius of the ring-segments. Summarizing, the reference grid $x_{\mathrm{ref}} = 60\,\mu\mathrm{m}$ for the ultrasonic test case deviates significantly from the values that have been obtained for the axisymmetric nozzle, $x_{\mathrm{ref}} = 181\,\mu\mathrm{m}$ and $x_{\mathrm{ref}} = 245\,\mu\mathrm{m}$ and is thus case-dependent.

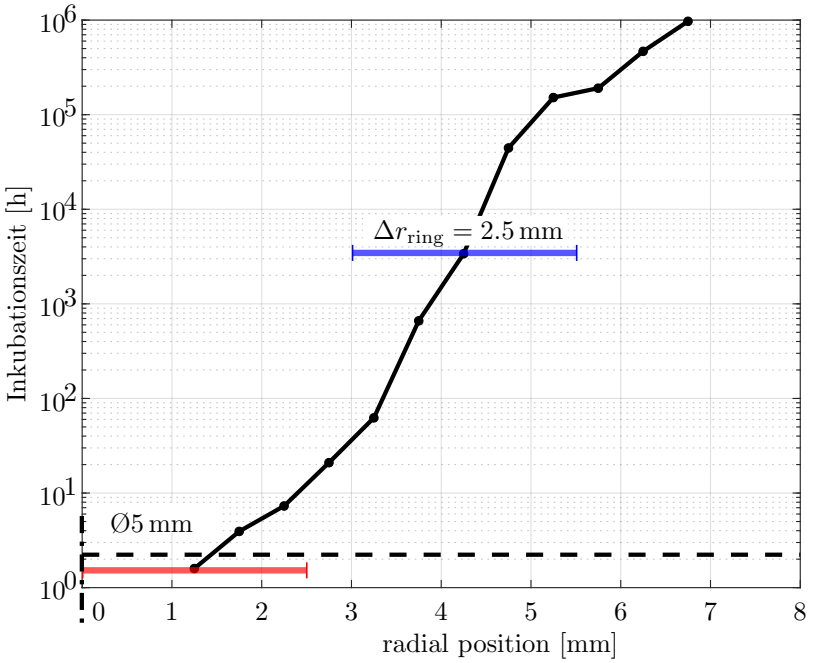

Figure 6: The radial distribution of the incubation time for the stationary specimen compared to the experimental value $t_{\mathrm{inc}} = 2.25\,\mathrm{h}$ (dashed line) measured by [18]. The exemplary ring width $\Delta r_{\mathrm{ring}} = 2.5\,\mathrm{mm}$ is shown in blue, resulting in a Ø5 mm area for $r = 1.25\,\mathrm{mm}$ (red).

5 CONCLUSION AND OUTLOOK

A method for the coupling of CFD collapse load collectives with a simple material model was presented and applied for the assessment of incubation time on two standardized test cases. We presented a method for the time extrapolation of the wall load to capture realistic time scales together with a step-by-step implementation guideline. We also pointed out limitations of the particular material model such as the neglect of loads below the materials yield strength and

suggest to consider material models that also take into account high-cycle fatigue mechanisms as well as strain-rate dependence of the material properties in further studies.

The scaling of collapse load collectives to a referenced grid showed that the reference grid parameter x_{ref} is case-dependent. A calibration of x_{ref} as proposed by [6], by pressure measurements and the exploitation of the grid dependence of the virtual sensor results, depends on the sensor size and does not seem to be generally valid. We conclude that the erosion model, i.e. coupled CFD – material model, comprises at least one model parameter that needs to be case-dependently fixed on measurement data. Thus, we suggest to consider a wider range of operation conditions and test cases in order to further figure out the significance of the model parameter x_{ref}.

For a more predictive method, the detailed spatial resolution of the multitude of single bubble collapses seems to be indispensable.

ACKNOWLEDGEMENTS

The authors wish to gratefully acknowledge the financial support by the Federal Ministry for Economic Affairs and Energy (BMWi) (Project ID 03SX454D). The authors also gratefully acknowledge the Gauss Centre for Supercomputing e.V. (www.gausscentre.eu) for providing computing time through the John von Neumann Institute for Computing (NIC) on the GCS Supercomputer JUWELS at Jülich Supercomputing Centre (JSC).

REFERENCES

[1] C. E. Brennen. *Cavitation and Bubble Dynamics*. Cambridge University Press, Cambridge (2013).

[2] J.-P. Franc. Incubation Time and Cavitation Erosion Rate of Work-Hardening Materials. *Journal of Fluids Engineering*, **131**:021303 (2009).

[3] J.-P. Franc, M. Riondet, A. Karimi, and G. L. Chahine. Material and velocity effects on cavitation erosion pitting. *Wear*, **274-275**:248–259 (2012).

[4] J.-P. Franc, M. Riondet, A. Karimi, and G. L. Chahine. Impact Load Measurements in an Erosive Cavitating Flow. *Journal of Fluids Engineering*, **133**:121301 (2011).

[5] M. S. Mihatsch, S. J. Schmidt, M. Thalhamer, N. A. Adams, R. Skoda, and U. Iben. Collapse detection in compressible 3-D cavitating flows and assessment of erosion criteria. *WIMRC 3rd International Cavitation Forum 2011* (2011).

[6] M. S. Mihatsch, S. J. Schmidt, and N. A. Adams. Cavitation erosion prediction based on analysis of flow dynamics and impact load spectra. *Physics of Fluids*, **27**:103302 (2015).

[7] M. S. Mihatsch. *Numerical Prediction of Erosion and Degassing Effects in Cavitating Flows*. Ph.D. thesis, TU München (2016).

[8] S. Mottyll. *Numerical 3D Flow Simulation of Cavitation at Ultrasonic Horns and Assessment of Flow Aggressiveness, Erosion Sensitive Wall Zones and Incubation Time*. Ph.D. thesis, Ruhr-Universität Bochum (2017).

[9] R. Skoda, U. Iben, A. Morozov, M. S. Mihatsch, S. J. Schmidt, and N. A. Adams. Numerical simulation of collapse induced shock dynamics for the prediction of the geometry, pressure and temperature impact on the cavitation erosion in micro channels. *WIMRC 3rd International Cavitation Forum 2011* (2011).

[10] P. Koukouvinis, G. Bergeles, and M. Gavaises. A new methodology for estimating cavitation erosion: Application on a high speed cavitation test rig. In *11th World Congress on Computational Mechanics (WCCM XI)* (2014).

[11] A. Peters, H. Sagar, U. Lantermann, and O. el Moctar. Numerical modelling and prediction of cavitation erosion. *Wear*, **338-339**:189–201 (2015).

[12] A. Peters, U. Lantermann, and O. el Moctar. Numerical prediction of cavitation erosion on a ship propeller in model- and full-scale. *Wear*, **408-409** (2018).

[13] ASTM-G32. Standard test method for cavitation erosion using vibratory apparatus. *ASTM International* (2008).

[14] A. Žnidarčič, R. Mettin, C. Cairós, and M. Dular. Attached cavitation at a small diameter ultrasonic horn tip. *Physics of Fluids*, **26**:023304 (2014).

[15] S. Mottyll and R. Skoda. Numerical 3D flow simulation of ultrasonic horns with attached cavitation structures and assessment of flow aggressiveness and cavitation erosion sensitive wall zones. *Ultrasonics Sonochemistry*, **31**:570–589 (2016).

[16] S. Mottyll and R. Skoda. Numerical 3D flow simulation of attached cavitation structures at ultrasonic horn tips and statistical evaluation of flow aggressiveness via load collectives. *Journal of Physics: Conference Series*, **656**:012052 (2015).

[17] S. Hattori and E. Nakao. Cavitation erosion mechanisms and quantitative evaluation based on erosion particles. *Wear*, **249**:839–845 (2001).

[18] S. A. Paepenmöller, J. Kuhlmann, M. Blume, and R. Skoda. Assessment of Flow Aggressiveness at an Ultrasonic Horn Cavitation Erosion Test Device by PVDF Pressure Measurements and 3D Flow Simulations. In *Proceedings of the 10th International Symposium on Cavitation (CAV2018)*, J. Katz, editor. ASME, New York, NY (2018).

[19] M. S. Mihatsch, S. J. Schmidt, and N. A. Adams. Estimation of incubation times through numerical simulation of 3-D unsteady cavitating flows. *SHF Conference* (2013).

[20] S. J. Schmidt, I. H. Sezal, and G. H. Schnerr. Compressible simulation of high-speed hydrodynamics with phase change. *European Conference on Computational Fluid Dynamics* (2006).

[21] S. J. Schmidt, I. H. Sezal, G. H. Schnerr, and M. Thalhamer. Riemann Techniques for the Simulation of Compressible Liquid Flows with Phase-transition at all Mach numbers - Shock and Wave Dynamics in Cavitating 3-D Micro and Macro Systems. *46th AIAA Aerospace Sciences Meeting and Exhibit* (2008).

[22] S. Mottyll, S. Müller, P. Niederhofer, J. Hussong, S. Huth, and R. Skoda. Analysis of the cavitating flow induced by an ultrasonic horn – Numerical 3D simulation for the analysis of vapour structures and the assessment of erosion-sensitive areas. *EPJ Web of Conferences*, **67**:02078 (2014).

[23] C. Deimel and R. Skoda. Implementation of an explicit density-based solver for the simulation of cavitating flows in OpenFOAM. *9th OpenFOAM Workshop, Zagreb, Croatia*.

[24] A. Harten. High resolution schemes for hyperbolic conservation laws. *Journal of Computational Physics*, **49**:357–393 (1983).

[25] H. Jasak, H. G. Weller, and A. D. Gosman. High resolution nvd differencing scheme for arbitrarily unstructured meshes. *International Journal for Numerical Methods in Fluids*, **31**:431–449 (1999).

[26] K.-H. Kim, G. Chahine, J.-P. Franc, and A. Karimi, editors. *Advanced Experimental and*

Numerical Techniques for Cavitation Erosion Prediction, volume 106 of *Fluid Mechanics and Its Applications*. Springer Netherlands, Dordrecht (2014).

[27] C. Kaufhold, F. Pöhl, S. Mottyll, R. Skoda, and W. Theisen. Numerical simulation of the deformation behavior of metallic materials under cavitation induced load in the incubation period. *Wear*, **376-377**:1138–1146 (2017).

[28] F. Pöhl, S. Mottyll, R. Skoda, and S. Huth. Evaluation of cavitation-induced pressure loads applied to material surfaces by finite-element-assisted pit analysis and numerical investigation of the elasto-plastic deformation of metallic materials. *Wear*, **330-331**:618–628 (2015).

[29] S. J. Schmidt, M. S. Mihatsch, M. Thalhamer, and N. A. Adams. Assessment of the Prediction Capability of a Thermodynamic Cavitation Model for the Collapse Characteristics of a Vapor-Bubble Cloud. *WIMRC 3rd International Cavitation Forum 2011* (2011).

[30] A. Karimi and W. R. Leo. Phenomenological model for cavitation erosion rate computation. *Materials Science and Engineering*, **95**:1–14 (1987).

[31] A. L. Gurson. Continuum theory of ductile rupture by void nucleation and growth: Part i—yield criteria and flow rules for porous ductile media. *Transaction of ASME*, **99** (1977).

[32] A. Needleman and V. Tvergaard. An analysis of ductile rupture in notched bars. *Journal of the Mechanics and Physics of Solids*, **32**:461 – 490 (1984).

[33] S. Hattori, T. Hirose, and K. Sugiyama. Prediction method for cavitation erosion based on measurement of bubble collapse impact loads. *Journal of Physics: Conference Series*, **147**:012011 (2009).

[34] S. Hattori, T. Hirose, and K. Sugiyama. Prediction method for cavitation erosion based on measurement of bubble collapse impact loads. *Wear*, **269**:507–514 (2010).